nature communications

Article

https://doi.org/10.1038/s41467-024-54202-4

Dyna-vivo-seq unveils cellular RNA dynamics during acute kidney injury via in vivo metabolic RNA labeling-based scRNA-seq

Received: 6 February 2024

Accepted: 1 November 2024

Published online: 14 November 2024

Check for updates

Kun Yin[1,2,5], Yiling Xu[2,5], Ye Guo[2,5], Zhong Zheng[1,5], Xinrui Lin[1], Meijuan Zhao[2], He Dong[2], Dianyi Liang[2], Zhi Zhu[2], Junhua Zheng[1] ✉, Shichao Lin[3] ✉, Jia Song[4] ✉ & Chaoyong Yang[1,2,3] ✉

A fundamental objective of genomics is to track variations in gene expression program. While metabolic RNA labeling-based single-cell RNA sequencing offers insights into temporal biological processes, its limited applicability only to in vitro models challenges the study of in vivo gene expression dynamics. Herein, we introduce Dyna-vivo-seq, a strategy that enables time-resolved dynamic transcription profiling in vivo at the single-cell level by examining new and old RNAs. The new RNAs can offer an additional dimension to reveal cellular heterogeneity. Leveraging new RNAs, we discern two distinct high and low metabolic labeling populations among proximal tubular (PT) cells. Furthermore, we identify 90 rapidly responding transcription factors during the acute kidney injury in female mice, highlighting that high metabolic labeling PT cells exhibit heightened susceptibility to injury. Dyna-vivo-seq provides a powerful tool for the characterization of dynamic transcriptome at the single-cell level in living organism and holds great promise for biomedical applications.

The dynamics of molecular components and networks in organisms are crucial for understanding biological processes[1]. Temporal gene expression measurements provide valuable insights into the dynamic behavior of biological systems[2]. However, several challenges remain. First, traditional ensemble-based samples, where the average of millions of cells in multicellular systems is measured, tend to blur the dynamics of genes in individual cells. Second, past and current measurements have been static. The destruction of cells provides only an instantaneous snapshot of the cellular state, which may not fully represent the dynamic processes occurring within the cells over time. Finally, the biochemical and genetic strategies to characterize the dynamics of genes are usually detached from normal cell physiology, leading to an incomplete reflection of the true transcriptional processes in living cells.

Recently, advanced single-cell RNA-sequencing (scRNA-seq) technology has been recognized as a powerful tool in revealing the heterogeneity of cellular states[3–5]. However, due to their destructive nature, standard scRNA-seq methods only capture a snapshot of gene expression, showing limitations in conveying information about temporal dynamics[6]. To address this limitation, computational trajectory inference orders cells by their transcriptome similarity to reveal biological progression[7,8]. Nevertheless, it cannot follow the same cell over time and typically demands prior biological knowledge to determine

[1]Institute of Molecular Medicine, Department of Urology, Renji Hospital, School of Medicine, Shanghai Jiao Tong University, Shanghai 200120, PR China. [2]The State Key Laboratory of Physical Chemistry of Solid Surfaces, MOE Key Laboratory of Spectrochemical Analysis & Instrumentation, Key Laboratory for Chemical Biology of Fujian Province, Department of Chemical Biology, College of Chemistry and Chemical Engineering, Xiamen University, Xiamen 361005, PR China. [3]Innovation Laboratory for Sciences and Technologies of Energy Materials of Fujian Province (IKKEM), Xiamen 361005, PR China. [4]Institute for Developmental and Regenerative Cardiovascular Medicine, Xinhua Hospital, Shanghai Jiao Tong University School of Medicine, Shanghai 200092, PR China. [5]These authors contributed equally: Kun Yin, Yiling Xu, Ye Guo, Zhong Zheng. ✉e-mail: zhengjh0471@sina.com; linscnano@xmu.edu.cn; songjiajia2010@shsmu.edu.cn; cyyang@xmu.edu.cn

the directionality of complex biological processes[9]. RNA velocity addresses this by tracking cell states using mRNA abundance derivatives[10,11]. However, velocity estimates are noisy due to the inefficiency of detecting the intronic sequences and are influenced by the splicing rates and intron stabilities[12,13].

To address these challenges, several metabolic RNA labeling approaches have been developed[14–16]. The integration of scRNA-seq with metabolic labeling of new mRNA molecules provides a more direct and precise measurement of gene expression changes over time. These approaches introduce a chemical tag, such as 4-thiouridine (4sU), into new RNA by exposing cells to nucleoside analogs[17]. Before sequencing, this tag is subsequently used to efficiently distinguish the newly synthesized RNAs from total RNAs by converting 4sU to a cytosine analog by chemical reagent such as alkylation-based iodoacetamide (IAA)[18], addition-elimination-based hydrazine hydrate ($N_2H_4{\cdot}H_2O$)[19], and oxidative nucleophilic-aromatic substitution-based trifluoroethanol/sodium periodate (TFEA/$NaIO_4$)[20]. Initially, scSLAM-seq[21] and NASC-seq[22] were developed to extend metabolic RNA labeling sequencing to single-cell resolution in combination with scRNA-seq. Nonetheless, these methods are low-throughput, high-cost, and labor-intensive, making it difficult to characterize large numbers of tissue cells. To improve throughput and efficiency, high-throughput barcoding strategies have been integrated into metabolic RNA labeling approaches to sequencing, leading to the development of sci-fate[23] and scNT-seq[20]. Despite these advancements, the high cell loss rate associated with these techniques can introduce bias in tissue cell detection, which shows limitations when applied to tissue models. To achieve a more accurate and comprehensive understanding of biological processes in complex organsims, it is crucial to develop a high-sentivity and high-throughput method that can capture RNA transcription dynamics in vivo, reflecting the true complexity and diversity of cellular responses in their natural environment.

Herein, we describe Dyna-vivo-seq, which combines Well-Paired-Seq2 (WPS2) and in vivo 4sU metabolic labeling, to faithfully record RNA dynamics in vivo at the single-cell level by simultaneously profiling new and old RNAs. Using Dyna-vivo-seq, we demonstrate the successful incorporation of 4sU into mouse kidney cells through intravenous injection without disturbing gene expression. The new RNAs can provide an extra dimension that aids in the discernment of cellular heterogeneity. Based on Dyna-vivo-seq, we reveal the heterogeneities of RNA dynamics among different cell types.

Remarkably, we find two distinct cellular states in proximal straight tubule (PST) and proximal convoluted tubule (PCT) cells, categorized by differential RNA turnover rates. Expanding the scope of Dyna-vivo-seq, we employ it to characterize temporally transcriptomic patterns in acute kidney injury (AKI), a significant global public health concern associated with 1.7 million deaths annually[24,25]. The characterization of early stage of AKI is critical for potential complication[26–28], which would play an important role in the early diagnosis and intervention treatment of AKI. By comparing old RNA with new RNA, we show that new RNA-based analysis more sensitively reveals AKI-stimuli responsive regulation. Taking advantage of enhanced sensitivity of new RNA-based analysis, we quantify the dynamics of 90 transcription factors (TFs) within ~5.3 h. Importantly, we observe that the high metabolic labeling PST and PCT cells are more sensitive to injury, compared to their low metabolic labeling counterparts. The Dyna-vivo-seq approach offers a powerful tool for the precise investigation of temporal transcription dynamics in vivo at the single-cell level, offering valuable insights into cellular responses to various stimuli and dynamic changes in gene expression programs.

Results

Overview of Dyna-vivo-seq

To enable accurate tracking of biological processes in vivo at the single-cell level, we have developed a method called Dyna-vivo-seq, which is based on the recently developed size-exclusion and locally quasi-static hydrodynamic microwell-based single-cell RNA sequencing platform, known as Well-Paired-Seq2[29]. The Dyna-vivo-seq method comprises the following key steps (Fig. 1): (i) Injection of biocompatible thymidine analog 4sU into mice via tail-intravenous injection. With the circulation of blood, 4sU rapidly diffuses throughout the entire body, including the kidney. Subsequently, the kidney tissue is dissociated into a single-cell suspension and then paired with barcoded beads in the chip. (ii) After the mRNAs from the lysed cells are captured by the barcoded beads, we recover the beads from the chip. After treatment with iodoacetamide (IAA), the 4sU in the mRNA molecules undergoes transformation into a cytosine analog by covalently attaching a carboxyamidomethyl-group to 4sU, resulting in variations in the base's hydrogen-bonding pattern. Consequently, the sites of 4sU exhibit T-to-C substitution at single-base resolution during the step of reverse transcription, and these can be read out by following cDNA amplification, library preparation, and sequencing. (iii) Finally, the fraction of newly synthesized transcripts of each gene in each cell is distinguished by T-to-C conversions. As a result, each cell is associated with two digital RNA expression matrices, representing new and old RNA. By concurrently profiling new and old RNAs, Dyna-vivo-seq enables an accurate depiction of gene expression dynamics in response to acute perturbation and cell fate changes in vivo.

Performance validation of in vivo metabolic labeling

To evaluate the performance of the 4sU-based in vivo metabolic labeling method for scRNA-seq, we conducted a comparative analysis with in vitro and in vivo labeling conditions (Fig. 2a). For the in vitro labeling method, renal cells were dissociated into a single-cell suspension and incubated with cell culture medium containing 4sU for 1.5 h. However, the T-to-C substitution (~ 0.6%, Fig. 2b) and new RNA labeling ratio (~ 1.5%, Fig. 2c) observed with the in vitro method were significantly lower than what has been reported in previous studies[20,30].

This suggests that the viability of renal cells may be severely affected when cultured in vitro, leading to abnormal RNA turnover rates. In contrast, the in vivo labeling method involved injecting the 4sU solution via the caudal vein. After a 1.5 h incubation, the kidney was extracted from the mouse and dissociated into a single-cell suspension within 15 min. Using the in vivo labeling method, we observed significantly higher T-to-C substitution (~ 2.0%, Fig. 2b) and new RNA labeling ratio (20.7%, Fig. 2c) compared to the in vitro labeling methods. This indicates that the in vivo approach better captures the dynamic RNA transcription within cells, due to the native physiological conditions. Additionally, gene expression in labeled cells exhibited a high correlation with that of the unlabeled cells (Pearson correlation coefficient $r = 0.91$), further demonstrating the excellent biocompatibility of the 4sU-based metabolic labeling in vivo (Fig. 2d). To demonstrate the homogeneous diffusion of 4sU in the kidney, we spatially dissected the kidney into four parts from top to bottom and performed sequencing analysis (Supplementary Fig. 1a). We found that the ratio of T-to-C substitution and new RNA labeling were almost identical across all kidney sections, indicating that 4sU diffuses uniformly throughout the whole kidney (Fig. 2e and Supplementary Fig. 1b). To assess whether in vivo 4sU metabolic labeling affects gene expression, we analyzed 24,237 labeled cells and 8891 unlabeled cells. The labeled and unlabeled cells were well integrated into the UMAP space after batch effect correction with Harmony (Fig. 2f).

Taken together, these results validate the effectiveness and biocompatibility of the in vivo 4sU-based metabolic labeling method for scRNA-seq. By faithfully capturing the dynamic RNA transcription in single cells without disturbing gene expression patterns, this method holds great promise for studying complex biological processes at the single-cell level in vivo.

Profiling the landscape of RNA dynamics in normal renal tissues

mRNA turnover is tightly regulated and involves a series of biochemical processes that can occur at various stages of the mRNA's

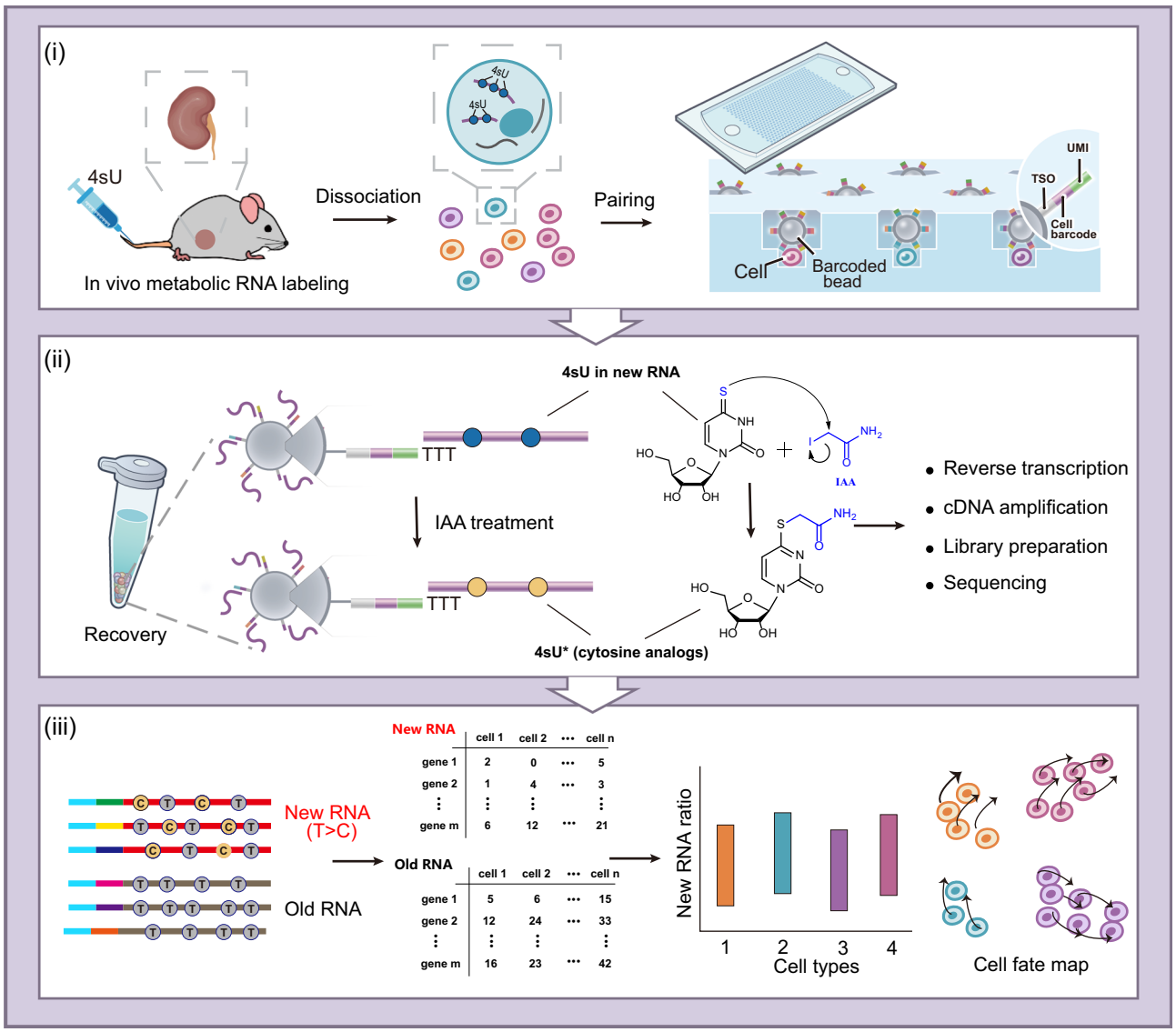

Fig. 1 | Workflow of Dyna-vivo-seq. i The thymidine analog 4sU is injected into mice via tail-intravenous injection and the labeled renal cells are paired with the barcoded beads in the size-exclusion and locally quasi-static hydrodynamic dual wells. **ii** The 4sU in the mRNA molecules are transformed into a cytosine analog after IAA treatment and read out by sequencing. **iii** Reads with T-to-C substitution(s) are identified as new RNAs while the remaining reads are identified as old RNAs. By concurrently profiling new and old RNAs in each cell, RNA turnover rates and cell fate map can be determined. Reprinted with permission from Kun Yin, Meijuan Zhao, Yiling Xu, Zhong Zheng, Shanqing Huang, Dianyi Liang, He Dong, Ye Guo, Li Lin, Jia Song, Huimin Zhang, Junhua Zheng, Zhi Zhu, and Chaoyong Yang. 2024. Well-Paired-Seq2: High-Throughput and High-Sensitivity Strategy for Characterizing Low RNA-Content Cell/Nucleus Transcriptomes. Anal. Chem. 96, 6301-6310. https://doi.org/10.1021/acs.analchem.3c05785). Copyright 2024 American Chemical Society. Source data are provided as a Source Data file.

life cycle, which are essential for maintaining cellular homeostasis and responding to changes in the cellular environment[31,32]. We profiled the landscape of mRNA turnover in renal tissues at the single-cell level. Generally, mRNAs with high turnover rates should exhibit a larger fraction of newly transcribed RNAs, as indicated by a larger fraction of reads with T-to-C substitution(s) in Dyna-vivo-seq data. Using Seurat analysis, we disentangled the cellular subpopulations and visualized the data in UMAP space, where we analyzed and categorized a total of 24,237 cells into 20 distinct cell clusters (Fig. 3a, c). The fractions of new RNAs in each cell (Fig. 3b) and cell type (Fig. 3d) were characterized. Indeed, we observed a heterogeneous labeling ratio in each cell type. Among the cell types, the B cell has the highest fraction of labeling RNA (35%), indicating the highest turnover rate in the B cell (Fig. 3d). Furthermore, to profile the landscape of RNA dynamics in renal tissue, we ranked the turnover rates in all cell types (21,231 genes) (Supplementary Fig. 1c, Supplementary Data 1).

Notably, we found both that the PCT and PST cells were divided into two subclusters with different labeling ratios (high metabolic labeling PCT (H-PCT) and low metabolic labeling PCT (L-PCT), high metabolic labeling PST (H-PST) and low metabolic labeling PST (L-PST) cells), as shown in Fig. 3b, d. To investigate the heterogenity of RNA dynamics, we focus on several specific markers expressed in PCT and PST cells, including *Acsm2*, *Miox*, *Atp11a*, *Slc7a12*, and *Aadat*. Based on the total or old RNAs, all these markers are homogeneously expressed in PST or PCT cells; thus, they cannot exhibit the difference in PCT and PST cells (Fig. 3e, f and Supplementary Fig. 1d–f). On the contrary, when mapping of new or the ratio of new-to-total RNAs of these markers in UMAP space, especially new RNAs, notable differences emerged in PCT and PST cells, with the exception of *Aadat* (Fig. 3e, f, and Supplementary Fig. 1d–f). These findings indicated that the dynamics of genes can serve as an additional dimension to facilitate the discernment of cellular heterogeneity, even among cells of the same type, providing a more precise means of characterization.

https://doi.org/10.1038/s41467-024-54202-4

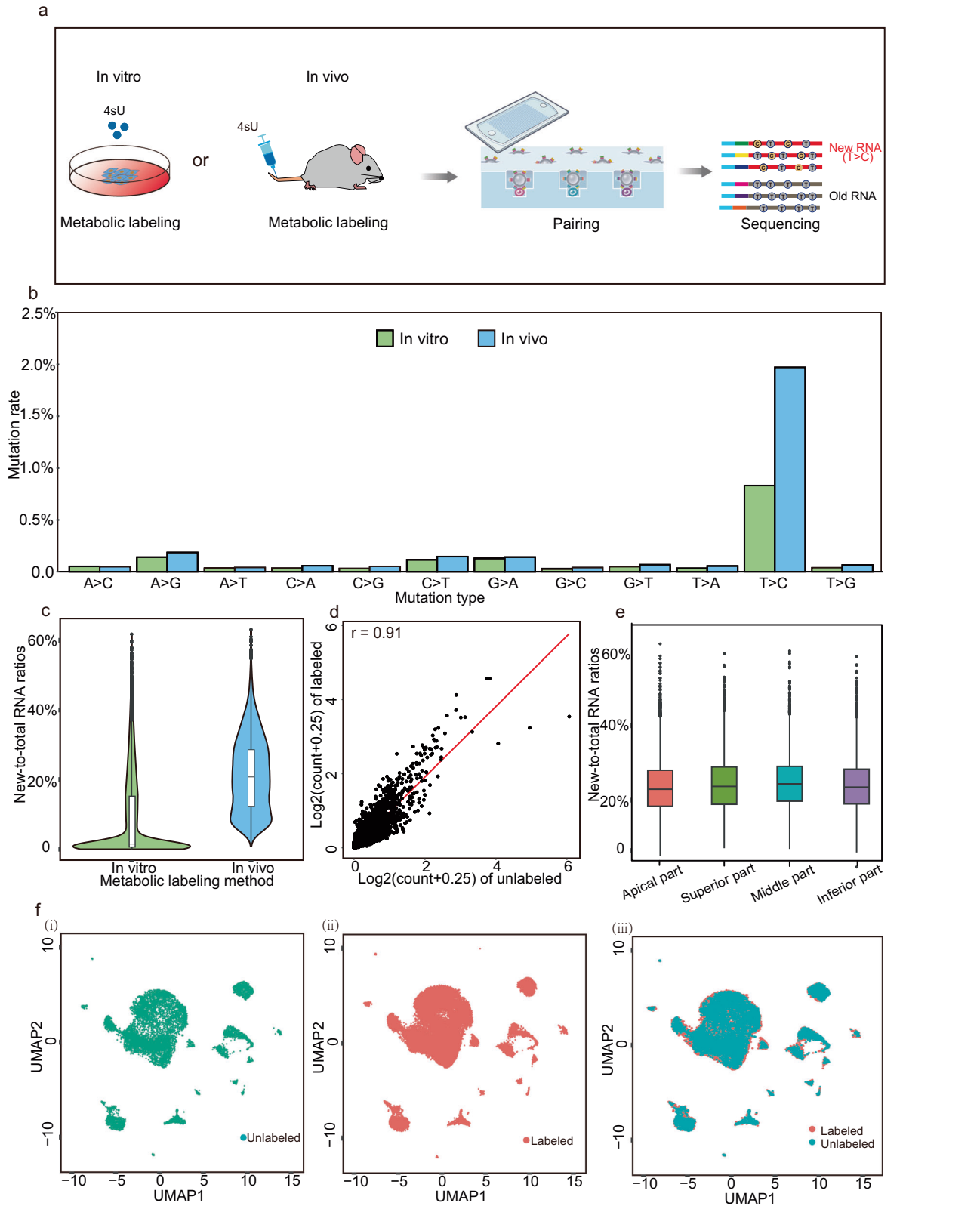

To investigate the difference between the two states of PST and PCT, we performed differential gene expression (DGE) analysis and Gene ontology (GO) enrichment analysis based on the new RNAs (Fig. 3g, h and Supplementary Fig. 1g, h). The differentially expressed genes were enriched in RNA splicing, response to metal ions, etc., indicating that the H-PT cells have a higher RNA turnover rate and higher activation for reabsorption of filtered load. Next, we investigated the cell-cell interactions among the renal cells by CellChat[33]. Consistently, when compared to L-PCT and L-PST cells, we noted that H-PCT and H-PST cells exhibit a greater enrichment of interactions involving ligand-receptor pairs with other cells (Fig. 3i). Taken together, Dynavivo-seq offers a comprehensive glimpse into the dynamics of mRNA turnover rate at the single-cell level and reveals cellular heterogeneity, functional activities, and intercellular communications.

Fig. 2 | Performance validation of in vivo metabolic labeling. a Experimental schemes of in vitro and in vivo metabolic labeling methods. Reprinted with permission from Kun Yin, Meijuan Zhao, Yiling Xu, Zhong Zheng, Shanqing Huang, Dianyi Liang, He Dong, Ye Guo, Li Lin, Jia Song, Huimin Zhang, Junhua Zheng, Zhi Zhu, and Chaoyong Yang. 2024. Well-Paired-Seq2: High-Throughput and High-Sensitivity Strategy for Characterizing Low RNA-Content Cell/Nucleus Transcriptomes. Anal. Chem. 96, 6301-6310. https://doi.org/10.1021/acs.analchem.3c05785). Copyright 2024 American Chemical Society. **b** Bar plot of substitution rates for in vitro and in vivo metabolic labeling methods. **c** Violin plot of the fraction of labeled transcripts per cell in 4sU-labeled renal cells based on in vitro and in vivo labeling methods. $n = 8891$ cells for in vitro group, $n = 24{,}237$ cells for in vivo group. **d** Scatter plot showing Pearson correlation between the revealed gene expression of unlabeled (x axis) and in vivo-4sU-labeled cells (y axis, from Dyna-vivo-seq). **e** Box plot showing the fraction of labeled transcripts per cell in 4sU labeled renal cells from the top (apical part) to bottom (inferior part). $n = 3813$ cells with 24.0% new-to-total RNA ratio for apical part, $n = 4829$ cells with 24.7% new-to-total RNA ratio for superior part, $n = 5036$ cells with 24.7% new-to-total RNA ratio for middle part, $n = 3633$ cells with 24.7% new-to-total RNA ratio for inferior part. Boxplots include centerline, median; box limits, upper and lower quartiles; and whiskers are highest and lowest values no > 1.5× interquartile range. **f** UMAP showing (i) unlabeled renal cells ($n = 8891$ cells) (ii) in vivo-4sU-labeled renal cells $n = 24{,}237$ cells and (iii) merged unlabeled and labeled cells using Dyna-vivo-seq. Source data are provided as a Source Data file.

Evaluating Dyna-vivo-seq performance for detecting injury-induced new RNAs in AKI

AKI is a clinical syndrome with complex pathogenesis and limited treatment methods[27]. Severe AKI can be life-threatening and increases the risk of chronic kidney disease (CKD) and mortality[27,34]. Renal ischemia-reperfusion injury (IRI) is one of the main causes of AKI[35]. Understanding the initiation of signaling events in acute perturbations is crucial for deciphering downstream signaling events, which can guide the development of clinical strategies for early intervention in AKI[24]. Recently, several researches have applied scRNA-seq to characterize the progressions of AKI, revealing the heterogeneous development in diverse cell subtypes[24,36–40]. Nevertheless, these methods show limitations in conveying information for the temporal dynamics of each cell and the initial hours of AKI have never been explored at the single-cell level.

Herein, we applied Dyna-vivo-seq to profile the RNA dynamics in each cell at the initial hours of AKI. To characterize the effect of labeling time on new RNA detection, we conducted metabolic labeling over a series of time intervals. As shown in Supplementary Fig. 2a, the T-to-C and new RNA ratios were 1.0%, 2.1%, 1.8% and 16.6%, 22.2%, and 28.1% for 30 min, 90 min, and 180 min labeling, respectively. The T-to-C ratio for the 30 min labeling was low, making it unsuitable for identifying new RNAs. Both 90 min and 180 min labeling had high T-to-C ratios and accurately identified new RNAs. However, since ischemia in this AKI model lasts less than 50 min, 180 min labeling would detect many non-ischemia-induced RNAs, reducing sensitivity. Therefore, we chose 90 min as the optimal labeling time for the subsequent AKI model. We performed uni-IRI surgeries on 10- to 12-week-old adult Balb/c mice and collected samples at multiple time gradients during disease progression. These time points included pre-ischemia (0 min), 30 min of ischemia, 50 min of ischemia, 50 min of ischemia followed by 3 h of reperfusion, and 50 min of ischemia followed by 4.5 h of reperfusion (Fig. 4a). First, we demonstrated that there was no batch effect between replicates (Supplementary Fig. 2c–e). In addition, the fractions of new RNAs in each sample were almost the same (Fig. 4b), demonstrating the similar metabolic labeling efficiency of each time point. According to the results of Seurat v4, we observed 27,590 cells by merging all samples (Supplementary Fig. 2f)

uni-IRI is usually associated with an inflammatory and oxidative stress response to ischemia and reperfusion which disturbs the kidney function. Many associated genes are induced to abnormal expression within a short time. Gene expression is tightly regulated by DNA-binding TFs. To quantify the activities of TFs in regulating gene expression, single-cell regulatory network inference and clustering (SCENIC) was applied[41]. Herein, we prioritized the new RNA-based SCENIC results, as they provide a more accurate representation of the regulatory response to AKI stimuli. Among them, 90 TFs showed significant changes in response to AKI in 13 cell types, as shown in Fig. 4c. With newly transcribed RNAs, SCENIC analysis revealed that many transcription factors were detected more rapidly in the two processes of ischemia and reperfusion, compared to old RNA-based SENIC analysis (Fig. 4c). For example, the hypoxia-related transcription factors of *Jun* (detected in high and low metabolic PCT and high metabolic PST cells), *Fos* (detected in low metabolic PCT, ENDO1, and CD-IC cells), and *Atf3* (detected in ENDO1, CD-IC, and Fib cells) increased rapidly during the ischemic stage, and the expression levels of these transcription factors decreased rapidly when the blood flow is restored. The inflammation-related TFs, such as *Cebpb* (detected in C1q+ Macro and C1q- Macro cells), *Nfkb1* (detected in Fib cells), and *Mafg* (detected in C1q+ Macro cells), upregulated rapidly during the reperfusion phase, indicating that an inflammatory response begins to occur in the renal tissue (Fig. 4d and Supplementary Figs. 3 and 4).

The heterogeneous RNA dynamics of proximal tubular cells in AKI

PT cells stand as the predominant cellular constituents within the kidney, entrusted with the pivotal role of reabsorbing nearly 65% of the filtered load[42]. The PT cells rely on oxidative mitochondrial metabolism to meet energy needs and have limited capacity for glycolysis, which makes them uniquely susceptible to damage during AKI. In the renal tissue, we unveiled the coexistence of two discrete cellular states distinguished by significantly different mRNA turnover rates within PST and PCT cells (Fig. 5a–c, and Supplementary Fig. 6a–c). The connection between RNA turnover rate and susceptibility to injury has never been explored. Herein, we characterized the relationship between vulnerability and RNA turnover rate in PT cells, categorized by high and low metabolic labeling, in the context of AKI.

First, we examined the dynamic transcriptional responses of PCT cells to AKI. Previous studies have illustrated an increased lipid deposition in the injured PT cells[43]. One notable protein, Plin2, also known as perilipin 2 or adipose differentiation-related protein, plays a crucial role as a lipid droplet surface protein and is an essential component of the PPAR signaling pathway[44]. As shown in Supplementary Fig. 6d, we found that *Plin2* is expressed in H-PCT cells after 3.8 h and 5.3 h reperfusion, which is consistent with RT-qPCR results of *Plin2* extracted from renal tissue at distinct process of AKI (Supplementary Fig. 6g). Subsequently, we conducted DEG analysis in Plin2+ and Plin2- PCT cells within the H-PCT, considering both new and old RNAs. Compared with the old RNA-based analysis, we observed significantly elevated expression in genes such as *Sgk1*, *Amotl2*, *Klf6*, *Ccn1*, *Adamts1*, *Angptl4*, *Gadd45a*, *Id3*, *Txnip*, *Pdk4*, *Ifrd1*, *Ehhadh*, *Myc*, *Nrg1*, *Trib1*, *Tnfrsf12a*, *Acot2*, *Mt1*, *Plin2*, and *Ptp4a1* in new RNA-based RNA analysis (Supplementary Fig. 6e). To gain insight into the functions of these enriched genes, we conducted a Gene Ontology (GO) analysis, which revealed their strong associations with various biological processes (such as thioester metabolic process, regulation of lipid metabolic process, reactive oxygen species metabolic process, etc.), underscoring their dysregulated H-PCT lipid metabolisms in the early stage of AKI (Supplementary Fig. 6f).

Tracking the fate of PST cells with Dyna-vivo-seq

Subsequently, we investigated the dynamic transcriptional responses of PST cells to AKI. To delineate the fate of PST cells in response to uni-IRI treatment, we employed dynamo, a recently established

https://doi.org/10.1038/s41467-024-54202-4

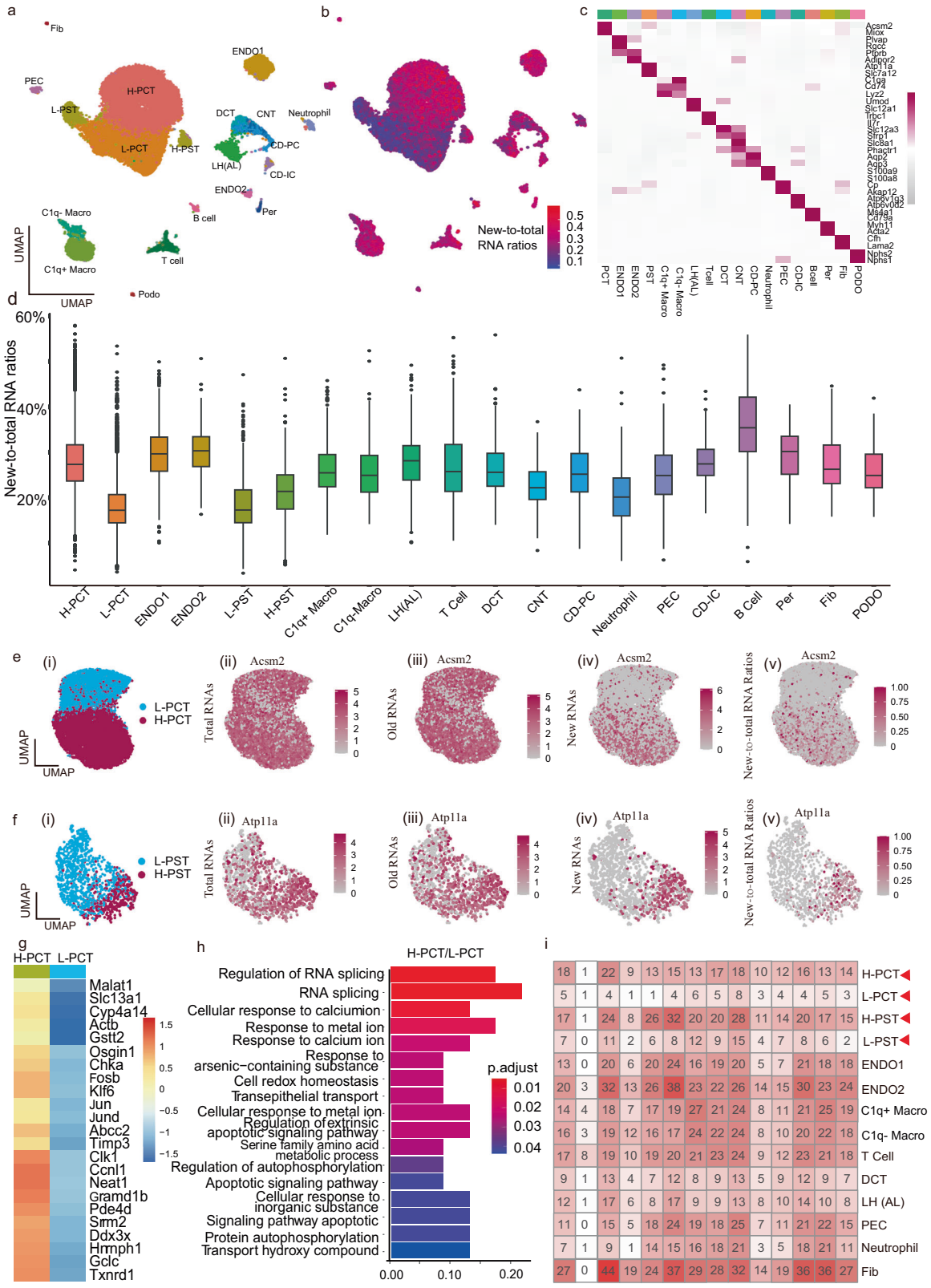

computational method, to analyze Dyna-vivo-seq data. RNA velocity can be inferred from scRNA-seq datasets through either a splicing-based model or a labeling-based model. The former estimates RNA velocity by discerning unspliced mRNAs (intronic reads) from spliced mRNAs (exonic reads). We examined the capability of the splicing-based RNA velocity model to predict the transcriptional trajectory of uni-IRI-treated single cells. However, our observations indicated poor consistency in the directionality of uni-IRI treatment-dependent transitions within the splicing-based RNA velocity vector flow (Fig. 5d).

Given the efficacy of metabolic RNA labeling in capturing rapid alterations in RNA abundance and quantifying newly synthesized RNAs unequivocally through unique molecular identifiers (UMIs), we reasoned that the paired measurements encompassing newly transcribed and old mRNAs from Dyna-vivo-seq could be employed to ascertain

Fig. 3 | The landscape of RNA dynamics in normal renal tissue. a UMAP of single-cell profiles (dots) from renal cells (24,237 cells) colored by cell type. PCT: proximal convolved tubule cell (including high metabolic labeling PCT (H-PCT) cluster and low metabolic labeling PCT (L-PCT) clusters); PST: proximal straight tubule cell (including high metabolic labeling PST (H-PST) clusters and low metabolic labeling PST (L-PST) clusters); ENDO1: endothelial cell 1; ENDO2: endothelial cell 2; C1q+ Marco: C1q+ macrophage cell; C1q- Marco: C1q- macrophage cell; LH(AL): thick ascending limb of the loop of Henle; DCT: distal convoluted tubule cell; CNT: connecting tubule cell; CD-PC: collecting duct principal cell; CD-IC: collecting duct intercalated cell; PEC: parietal epithelial cell; Per: pericyte cell; Fib: fibroblast cell; PODO: podocytes. **b** UMAP showing the fraction of labeled transcripts per cell in in vivo 4sU-labeled renal cells. **c** Heatmap showing the specific markers of each cell type. **d** Box plot showing the fraction of labeled transcripts in each cell type. $n_{H\text{-}PCT} = 10053$, $n_{L\text{-}PCT} = 6476$, $n_{ENDO1} = 1528$, $n_{ENDO2} = 188$, $n_{L\text{-}PST} = 870$, $n_{H\text{-}PST} = 382$, $n_{C1q^+\ Marco} = 1410$, $N_{C1q^-\ Marco} = 378$, $n_{LH(AL)} = 771$, $n_T = 586$, $n_{DCT} = 385$, $n_{CNT} = 96$, $n_{CD\text{-}PC} = 230$, $n_{Neutrophil} = 275$, $n_{PEC} = 176$, $n_{CD\text{-}IC} = 121$, $n_B = 118$, nPer=79, $n_{Fib} = 74$, $n_{Pod} = 42$. Boxplots include centerline, median; box limits, upper and lower quartiles; and whiskers are highest and lowest values no >1.5× interquartile range. **e** UMAP plot based on high variation genes of H- and L-PCT cells (i), total RNAs (ii), old RNAs(iii), new RNAs(iv), and new-to-total RNAs(v) of *Ascm2*. **f** UMAP plot based on high variation genes of H- and L-PST cells (**i**), total RNAs (ii), old RNAs(iii), new RNAs(iv), and new-to-total RNAs(v) of *Atp11a*. **g** Heatmap showing new RNA levels of significantly up-regulated genes between H-PCT and L-PCT. **h** Bar plot showing functional enrichments by GO analysis based on the up-regulated genes from (**g**). Statistical significance was determined by one-sided hypergeometric test. **i** CellChat showing significantly enriched ligand-receptor pairs among the 14 cell types. Source data are provided as a Source Data file.

metabolic labeling-based RNA velocity. As expected, the adoption of the labeling-based model yielded coherent velocity flows, perceptible in the low-dimensional embedding, depicting the transition from untreated cells to uni-IRI-treated cells. Metabolic labeling-based RNA velocity, as inferred from Dyna-vivo-seq data, recapitulated the temporal trajectory of gene expression alterations within single cells following uni-IRI treatment (Fig. 5e). This encompassed the initial phase movement observed during ischemia and the subsequent phase movement manifesting during reperfusion. We further extended this analysis to encompass L-PST cells, also employing a metabolic-based model for RNA velocity estimation (Fig. 5f). Results unveiled a distinctive lack of discrimination between the processes of ischemia and reperfusion, suggesting a comparatively lesser impact of RNA expression changes during AKI when contrasted with high metabolic labeling PST cells.

Havcr1 is a typical marker gene for injured PST cells[24]. To evaluate the injury state of PST cells, we characterized the expression level of newly synthesized *Havcr1* in H- and L-PST cells (Fig. 5g). We found that newly synthesized *Havcr1* was highly expressed in H-PST cells during the reperfusion process, which is consistent with the results of RT-qPCR of *Havcr1* extracted from renal tissue at the distinct process of AKI (Fig. 5g, Supplementary Fig. 6h). We also observed that the level of new *Havcr1* surpassed the diagonal steady-state line in the phase portraits. This departure from equilibrium signifies a pronounced shift in expression dynamics, indicating an acceleration in *Havcr1* expression (Fig. 5h). This observation was further substantiated through velocity analyses conducted within a low-dimensional embedding, where heightened velocity profiles align with the enhanced expression kinetics of *Havcr1* (Fig. 5i). These results demonstrated that the expression dynamics of *Havcr1* were enhanced within H-PST cells during the phase of reperfusion.

In addition, a concurrent presence of hypoxia and inflammation is commonly observed during AKI. Employing the SCENIC analysis, we observed that a hypoxia-inducible component, *Jun*[45], and an inflammatory-responsive transcription factor, *Cebpd*[46], exhibited pronounced changes. *Jun* is a crucial transcription factor belonging to the Activator Protein 1 (AP-1) family, which plays a significant role in cellular responses to hypoxia. It is sensitively responsive to changes in oxygen levels and can initiate gene expression changes that aid in cellular response and adaptation to the hypoxic microenvironment. *Cebpd* contributes to the regulation of immune and inflammatory pathways by modulating the expression of genes involved in cytokine production, immune cell recruitment, and tissue remodeling. Benefiting from the high sensitivity of Dyna-vivo-seq, we can provide insights into the AKI-induced hypoxia and inflammatory responses of *Jun* and *Cebpd* TF activation in the early stage of uni-IRI treatment.

Compared to the old RNA-based analysis, we found that the new expression of *Jun* is more significantly enhanced in the process of ischemia, while it was promptly attenuated upon restoration of renal blood circulation (Fig. 5j). With regards to the *Cebpd*, we unveiled a more significant increment of new expression over a 5.3 h timespan during AKI (Fig. 5k). Thrombospondin-1 (Thbs1) is a homotrimeric glycoprotein, which is primarily released by activated platelets and is involved in the promotion to AKI[47]. Consistently, we observed the activation of the THBS signaling pathway network, primarily driven by the Thbs1 ligand in combination with other receptor pairs (as shown in Supplementary Fig. 6i), after 3.8 h of uni-IRI treatment. Additionally, the interactions among H-PST cells were strengthened after 5.3 h of uni-IRI treatment based on the new RNA-based analysis (Fig. 5l). Taken together, our findings demonstrated that the sensitivity of Dyna-vivo-seq platform allows for a nuanced understanding of intricate cellular responses in the process of AKI.

Discussion

In this study, we introduce a strategy, termed "Dyna-vivo-seq", which enables temporal scRNA-seq by concurrently profiling both newly synthesized and old RNAs through 4sU labeling, employing the WPS2 platform. Before developing Dyna-vivo-seq, although nucleoside analog-based labeling methods have been integrated with scRNA-seq, such as scNT-seq, sci-fate, and Well-TEMP-seq, these methodologies have been confined to in vitro cell culture models, thereby failing to capture the authentic dynamics of RNAs in vivo. By harnessing an in vivo RNA labeling method, Dyna-vivo-seq offers unprecedented insights into temporal RNA dynamics within intricate and dynamic biological systems at single-cell resolution.

To verify the robustness of Dyna-vivo-seq, we conducted comparisons of in vivo metabolic labeling scRNA-seq (Dyna-vivo-seq), in vitro metabolic labeling scRNA-seq and non-labeling scRNA-seq. We demonstrated that in vivo metabolic labeling is significantly superior compared to in vitro metabolic scRNA-seq, and it does not significantly disrupt gene expression. Through the application of Dyna-vivo-seq, we characterized the landscape of RNA dynamics in kidney tissue. We executed an assessment of the turnover rate of 21,231 genes across diverse cell types, allowing us to rank their dynamics. Notably, we discerned two distinct states within PST and PCT cells, each exhibiting differential RNA turnover rates and cell-cell interactions. Based on the DEG and GO analyses, we observed an enrichment of biological functions related to the response to metal ions. This suggests that H-PT cells may play a primary role in responding to the reabsorption of filtered loads in the kidney.

Additionally, we characterized RNA dynamics during the early stages of AKI, a critical period that shapes subsequent AKI development. Our utilization of new RNAs enabled the identification of 90 TFs that were significantly responsive during ischemia and reperfusion. In comparison with the analysis on old RNA, we can more quickly detect inflammatory and hypoxia-associated TFs, such as *Jun*, *Atf3*, *Cebpb*, etc. This capability can be instrumental in informing early intervention strategies. Of particular interest, our observations revealed that H-PST and H-PCT cells are more susceptible to injury when compared to their counterparts, L-PST and L-PCT cells, suggesting that reducing the

https://doi.org/10.1038/s41467-024-54202-4

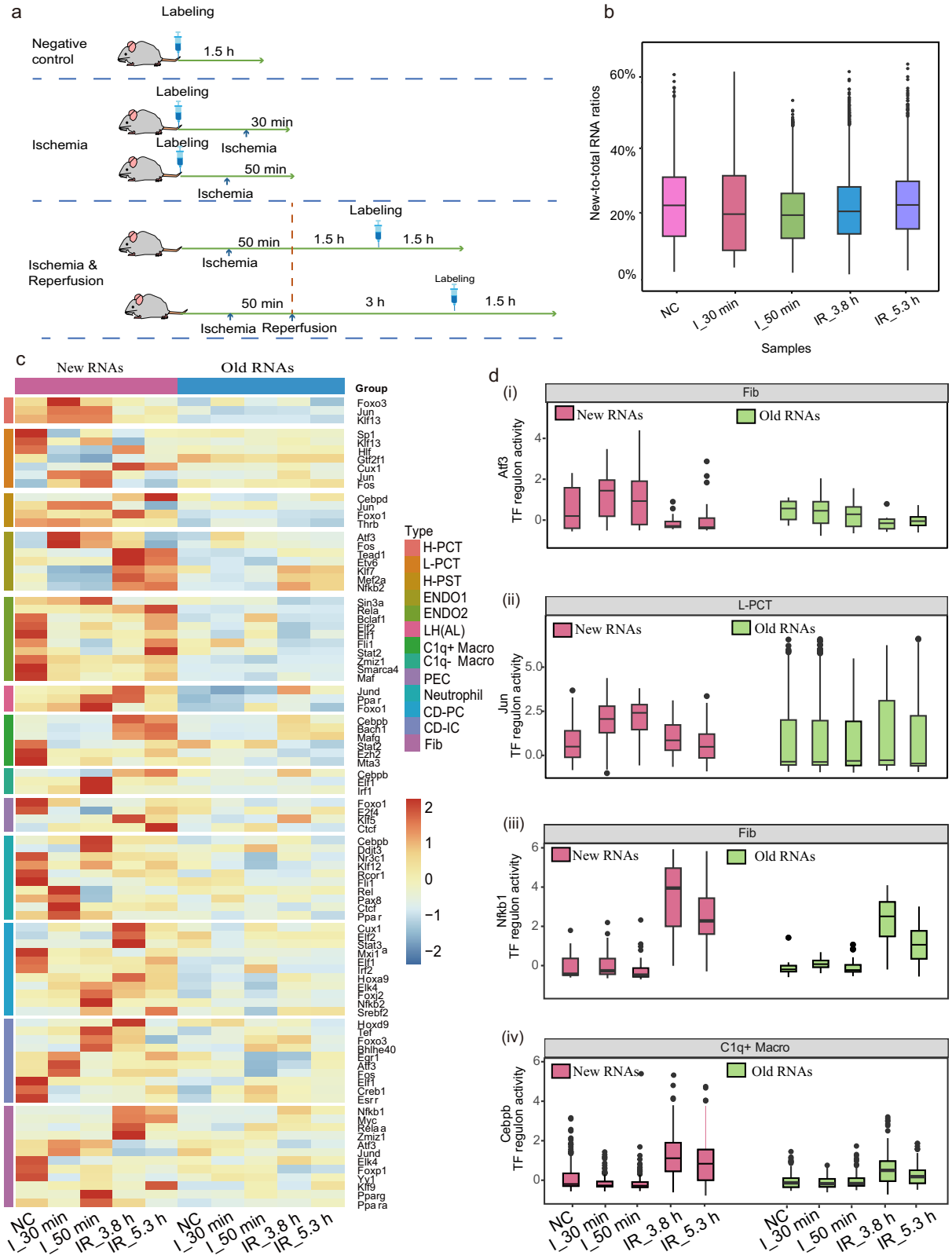

metabolic activity of RNAs may be a potential approach to mitigate AKI-induced injury in various clinical surgical scenarios, including kidney transplantation, partial nephrectomy, and renal artery angioplasty.

Based on the WPS2 platform, Dyna-vivo-seq ensures high capture efficiency and recovery of cells and high sensitivity of gene detection based on the size-exclusion and quasi-static hydrodynamic chip and the modified procedures of library preparation, making Dyna-vivo-seq superior to other metabolic RNA labeling based scRNA-seq methods, such as Well-TEMP-seq, scSLAM-seq, NASC-seq, scEU-seq, sci-fate, and scNT-seq (Supplementary Data2). Furthermore, the streamlined workflow can be executed using a simple chip and pipette setup, with an economical cost of less than US$0.10 per cell for library preparation. This renders the platform amenable to rapid and cost-effective implementation within standard biology laboratories.

Fig. 4 | Assessing the performance of Dyna-vivo-seq in detecting activity-induced new RNAs in AKI. a Experimental schemes of uni-IRI surgeries at distinct time points during disease progression. **b** Box plot showing the fraction of labeled transcripts in each point. $n = 3166$ cells for NC group, $n = 6323$ cells for I_30 min group, $n = 2526$ cells for I_50 min group, $n = 3692$ cells for IR_3.8 h group, and $n = 5001$ cells for IR_5.3 h group. Boxplots include centerline, median; box limits, upper and lower quartiles; and whiskers are highest and lowest values no >1.5× interquartile range. **c** Heatmap showing regulon activity of 90 TFs in response to distinct time points in 13 cell clusters, concurrently inferred from either new or old RNAs. TFs with fold change in average AUC value > 1.5 and adjusted P-value < 0.05 were considered as having differential regulatory activity. Statistical significance was determined by two-sided Wilcoxon test. It is worth mentioning that the results might be skewed by the cell numbers (Supplementary Fig. 5). **d** Box plots showing cell-type-specific regulon activity (inferred from either new or old RNAs) of *Atf3*, *Jun*, *Nfkb1*, and *Cebpb* at distinct time points. $n = 154$ for Fib cells, $n = 4428$ for L-PCT cells, $n = 1579$ for C1q+ Macro cells. Boxplots include centerline, median; box limits, upper and lower quartiles; and whiskers are highest and lowest values no > 1.5× interquartile range. Source data are provided as a Source Data file.

The successful integration of in vivo labeling strategies with scRNA-seq presents progress for addressing pivotal biological inquiries. For instance, this integrated approach has the potential to unravel intricate biological phenomena, including embryo development, tumor evolution, pathogen infection, etc. Furthermore, future developments that involve novel exogenous nucleoside analogs to facilitate additional conversions (e.g., 6-thioguanine for G-to-A conversion induction) in the context of Dyna-vivo-seq could enable independent recordings of diverse transcriptional processes within individual cells. By strategically coupling metabolic labeling with spatial transcriptomics methodologies, researchers can harness the power of both techniques to obtain a holistic understanding of how gene expression patterns evolve across both time and space.

Methods

Ethical statement

All animal experiments were conducted under the guidelines approved by the Institutional Animal Care and Use Committee of Xiamen University Laboratory Animal Center (reference number XMULAC20210044).

4-Thiouridine labeling

A 4sU solution with a concentration of 80 mg/mL was employed for labeling purposes. The solution was prepared by dissolving 80 mg of 4sU (Aladdin, cat# T122953) in 50 μL of DMSO (MP Biomedicals, cat# 196055) and subsequently diluting it to a final volume of 1 mL with 0.9% NaCl (Thermo Fisher, cat# AM9760G). The 4-thiouridine solution was administered to female Balb/c mice (10–12 weeks old, JiangSu GemPharmatech Co., Ltd) via tail vein injection, with the injection volume being calculated based on the respective weight of the mice. Specifically, a dosage of 10 μL per gram of body weight was administered for both normal and AKI mice. Metabolic labeling was conducted for a duration of 1.5 h. Upon completion, kidney tissue was extracted and preserved in tissue storage solution (Miltenyi Biotec, cat# 130-100-008).

Experimental procedures for ischemic acute kidney injury in mice

Initially, 10 to 12-week-old female mice were anesthetized via intraperitoneal injection using 30 mg/mL pentobarbital sodium. Renal ischemia was induced by temporarily occluding the renal artery with a vascular clamp, thereby restricting blood flow to the kidney. Subsequently, reperfusion was facilitated by removing the vascular clamp. During the ischemic phase, the renal artery was clamped for durations of 30 min (two replicates) and 50 min, respectively. Following clamp removal, the injured kidney was promptly extracted to prepare a single-cell suspension. For the reperfusion phase, the renal artery underwent clamping for a duration of 50 min, after which the clamp was removed to restore bloodstream circulation in the kidney. Then, the injured kidney was collected at two distinct time points: 3 h (two replicates) and 4.5 h (two replicates) following the initiation of reperfusion.

Tissue dissociation

The dissociation of renal tissues followed the dissociation protocol outlined in the Multi Tissue Dissociation Kit2 (Miltenyi Biotec, cat# 130-110-203). Briefly, a gentle MACS C tube was utilized, into which 4.8 mL of Buffer X, 50 μL of Enzyme P, 50 μL of Buffer Y, 100 μL of Enzyme D, and 20 μL of Enzyme A were added. Approximately one-fourth of the kidney tissue was then introduced into the gentleMACS C tube. The program's gentle MACS program Multi_E_01' was selected for the 15 min dissociation process. The sample was subsequently resuspended and filtered through a 100 μm strainer (Thermo Fisher, cat# 22363549). The filtrate underwent centrifugation at 300 × g for 10 min; the supernatant was discarded, and the pellet was resuspended in Red Blood Cell Lysis Buffer (Thermo Fisher, cat# 00-4300-54) to eliminate red blood cells. The cell count and viability were determined using a cell counter (Invitrogen, cat# C10283). The cell suspension was then diluted to achieve an approximate concentration of 250 cells per microliter.

Single cells/beads isolation

Initially, 110 μL of a diluted cell suspension was introduced into the chip, enabling cell capture through cell-capture wells by gravity. Subsequently, barcoded beads suspended in 20 × TE (Sigma, cat# V900840) were loaded into the chip and captured by bead-capture-wells. After removing excess barcoded beads with 20 × TE, a solution of 5% (w/v) surfactant aggregates (sodium lauroyl sarcosine, Solarbio, cat# S8100-25g) in mineral oil was injected into the chip. The surfactant settled in the wells, leading to cell lysis, and the released mRNA from cells were captured by the paired barcoded beads. Following a 15 min incubation on ice, the barcoded beads were recovered into a 1.5 mL centrifugal tube. Then, these barcoded beads were washed twice with 6× SSC (Thermo Fisher, cat# 15557044) and once with 50 mM PBS.

IAA treatment

This step utilized IAA (TCI, cat# TCI-I0741-5G) to convert 4sU to cytosine analogues. First, 100 μL 5 mM IAA (mixed with 50 mM PBS (pH=8.0) and 10% DMSO) was added to the centrifugal tube containing the barcoded beads, and the reaction was carried out at 37 °C for 60 min. Following the incubation, the barcoded beads underwent two washes with 50 mM PBS and one wash with 1 × RT buffer (Thermo Fisher, cat# EP0753).

Reverse transcription

The barcoded beads were then resuspended in a reverse transcription mix, consisting of 1× RT buffer, 1 mM dNTP (TransGen Biotech, cat# AD101-12), 2.5 μM Template Switch Oligo (Sangon, 5'-AAGCAGTGGTATCAACGCAGAGTGAATrGrGrG-3'), 1U/μL Recombination RNase Inhibitor (TaKaRa, cat# 2313 A), 10 U/μL reverse transcription enzyme (Thermo Fisher, cat# EP0753), 1 mM GTP (Thermo Fisher, cat# R0461), and 5% PEG-8000 (Beyotime, cat# R0056). The tube was then incubated at 42 °C for 90 min.

Exonuclease I treatment

The barcoded beads were subjected to a series of washes using TE-SDS (1 × TE and 0.5% SDS, Thermo Fisher, cat# AM9820), TE-TW (1 × TE and 0.01% Tween-20, Sigma, cat# P1379), and Tris-HCl (pH = 8.0, Invitrogen, cat# 15568025). Subsequently, they were resuspended in an Exonuclease I mixture (NEB, cat# M0293S) and incubated at 37 °C for 45 min.

https://doi.org/10.1038/s41467-024-54202-4

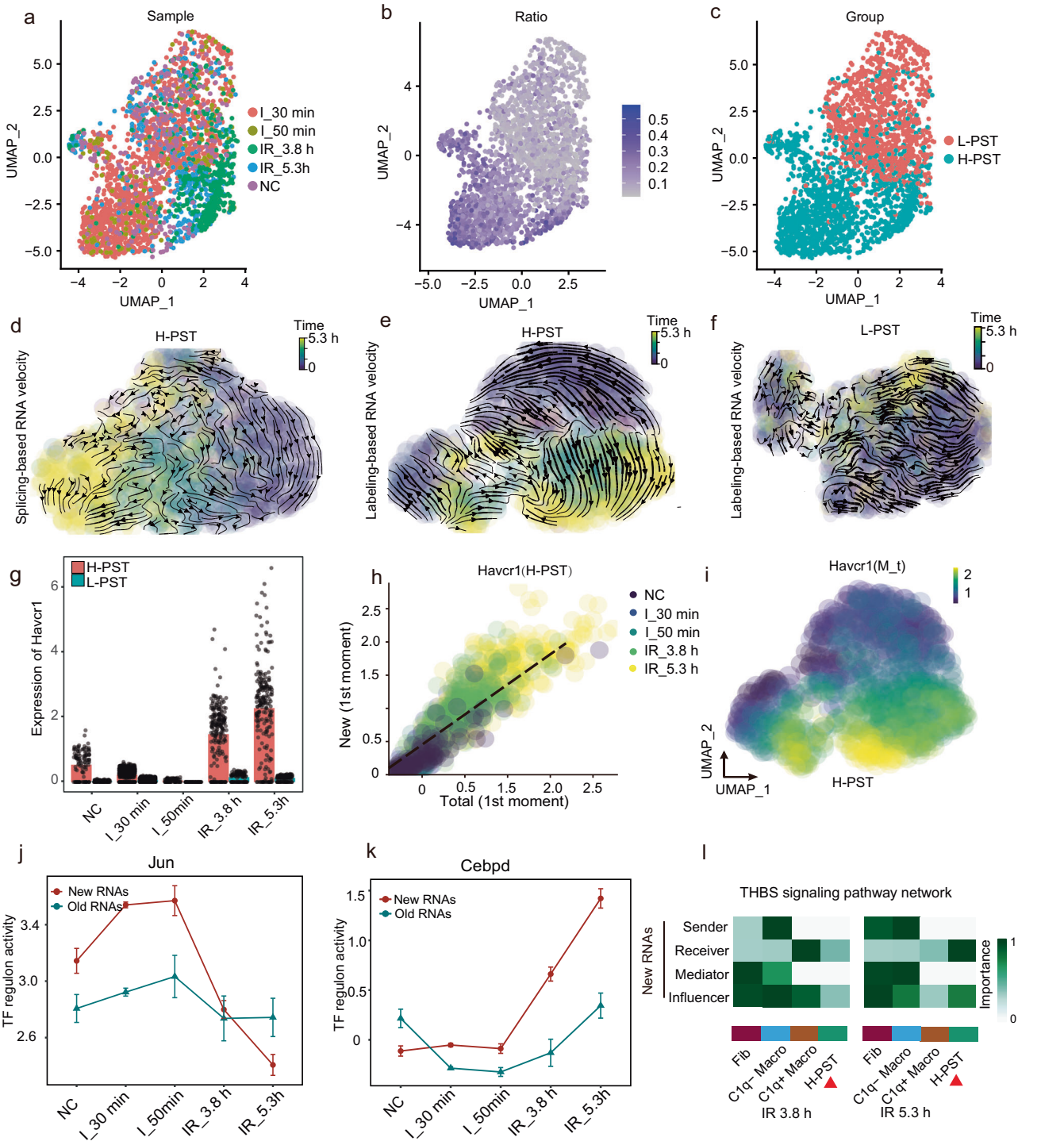

Fig. 5 | The heterogeneous responses in H-PST and L-PST cells during AKI. **a** UMAP showing PST cells from distinct time points. **b** UMAP showing the fraction of labeled transcripts per cell in vivo 4sU-labeled PST cells. **c** UMAP showing H-PST and L-PST cell clusters. UMAP visualization of H-PST cells responded to uni-IRI for distinct time points characterized by conventional splicing-based (**d**) or metabolic labeling-based RNA velocity analysis (**e**). Cells are color-coded by treatment time. The streamlines reveal the integration paths of local projections moving from the observed state to the extrapolated future state. **f** UMAP visualization of L-PST cells responded to uni-IRI for distinct time points characterized by metabolic labeling-based RNA velocity analysis. **g** Bar plot showing the expression of *Havcr1* in H-PST and L-PST cells at distinct time points. $n = 2240$ cells for L-PST, $n = 973$ for H-PST. Data shown as mean ± SD. **h** Phase portraits showing total-new RNA planes of *Havcr1*. **i** UMAP plots colored by smoothed total RNA level based on local averaging. The regulon activity of transcription factors *Jun* (**j**) and *Cebpb* (**k**) along with the AKI progression. In new RNA-based analysis, $n = 114$, 870, 79, 241, and 251 cells for NC, I_30 min, I_50 min, IR_3.8 h, and IR_5.3 h groups; In old RNA-based analysis, $n = 54$, 708, 44, 19, and 32 cells for NC, I_30 min, I_50 min, IR_3.8 h, and IR_5.3 h groups. Data shown as mean ± SD. **l** Signaling pathway role heatmap showing THBS signaling pathway network in Fib, C1q- Macro, C1q+ Macro, and H-PST cells. Source data are provided as a Source Data file.

Second strand cDNA synthesis and amplification

Initially, the barcoded beads were treated with 0.1 M NaOH for 5 min. Following thorough cleaning, the microspheres were resuspended in the second strand synthesis mixture, comprising 1× Maxima reverse transcription buffer, 1 mM dNTP, 12% PEG-8,000, 500 nM S3-primer (Sangon, 5′-AAGCAGTGGTATCAACGCAGAGTGAATG 3′), and 0.5 U/μL Klenow Exo- (NEB, cat# M0212L). The mixture was then incubated at 37 °C for 1 h. Next, every 10,000 microspheres were resuspended in 40 uL amplification mixture containing 1 × KAPA Hotstart HiFi ReadyMix (Roche, cat# KK2602) and 1 μM ISPCR oligo (Sangon, 5′-AAGCAGTGGTATCAACGCAGAGT-3′).

Library preparation

The amplified samples were purified twice with 0.6× DNA Clean Beads (Vazyme, cat# N411-02). Subsequently, for library construction, the appropriate Vazyme Kit (1 ng, 5 ng, 50 ng) (Vazyme, cat# TD-502) was chosen based on the sample concentration, following the manufacturer's instructions.

Total RNA extraction from tissues

The renal tissue was diced into small pieces, approximately 1 mm^3 in size. Subsequently, 1 ml of TRNzol Universal Reagent (TIANGEN, cat#4992730) was added to the tissue. The mixture was vortexed for 45 seconds, followed by a 5 min incubation at room temperature. The tissue was then centrifuged at 12,000 g for 5 min, and the resulting supernatant was carefully transferred to a new centrifuge tube. Then, 200 μL of chloroform (HUSHI, cat# 10006818) was added and the mixture was allowed to stand at room temperature for 2 min. The mixture was then centrifuged at 12,000 g for 10 min. The supernatant was transferred to a new centrifuge tube, and an equal volume of isopropanol (HUSHI, cat# 80109218) was added. After gently mixing the solution by inverting the tube 5-10 times, it was incubated on ice for 5 min and centrifuged at 12,000 g for 5 min. The supernatant was carefully removed, and 70% ethanol was added. After gently flicking the centrifuge tube and centrifuging at 7500 g for 3 min, this step was repeated once. After removing the supernatant and allowing the precipitate to air dry for approximately 5–10 min, DEPC-treated water was added to dissolve the precipitate.

Quantitative reverse transcription PCR (RT-qPCR)

The quantitative analysis of kidney injury biomarkers was performed using RT-qPCR. Reverse transcription was carried out using the HiScript III RT SuperMix (Vazyme, cat# R323). For qPCR, Taq Pro Universal SYBR qPCR Master Mix (Vazyme, cat# Q712) was utilized, following the manufacturer's instructions. DNA sequences used in this section are provided in Supplementary Table 1.

Alignment and Quantification of Metabolically Labeled Transcripts

Cell barcode (bases 1-12) and unique molecular identifier (UMI, bases 13-20) information from Read 1 of each read pair were extracted and subsequently tagged to Read 2 using the Drop-seq pipeline (v2.4.0)[3]. Adapter sequences and polyA tails were identified and trimmed, resulting in trimmed reads in bam format. These trimmed reads were then aligned to the mouse reference genome assembly (GRCm38, ENSEMBL release v98) using the STAR v2.7.3a workflow[48]. In addition, both exonic and intronic regions that mapped to annotated gene loci were retained for downstream analysis.

The scNT-seq pipeline[20] was used to quantify the labeled and unlabeled transcripts. For each cell, uniquely mapped sequences with mapping scores >10 were grouped by UMI indices and were used to determine the T-to-C substitution(s) using sam2tsv (https://github.com/lindenb/jvarkit/). T-to-C substitution(s) with base Phred quality scores >27 were retained. In the control group (without 4sU labeling and IAA treatment), we identified sites with T-to-C substitutions to serve as background mutations. These were then utilized to correct mutations within the experimental group. The labeled reads (new transcripts) were identified by at least one T-to-C substitution(s). For each gene, the total numbers of unique labeled and unlabeled transcript sequences were separately counted and assembled into matrices with gene names as rows and cell barcodes as columns. Finally, each cell was associated with two digital gene expression matrices (labeled or unlabeled transcripts) from the Dyna-vivo-seq sequencing data.

Cell type identification of renal tissue samples

The raw gene count matrices based on total UMI for each sample were first processed using the R packages SoupX[49] and DoubletFinder[50] to remove ambient RNA and doublets. The pre-processed normal renal tissue samples and acute kidney injury tissue samples were then separately merged into two Seurat objects using R package Seurat (v4.3.0)[51] for downstream analysis. Cells with gene detection in > 5% of cells and with a low-count ratio of UMIs mapped to mitochondrial genes (< 25%) were retained. Furthermore, cells containing more than 500 detected genes were preserved in normal renal tissues. The quality-controlled Seurat objects were normalized using the default parameters of the NormalizeData function. The top 2000 highly variable genes (HVGs) were identified using the "vst" method of the FindVariableFeatures function. The expression levels of HVGs in cells were then scaled and centered, and the top 30 principal components were selected after principal component analysis using the RunPCA function. For the normal renal tissue data, Harmony[52] was used with default parameters for data integration after principal component analysis. Then, runUMAP and FindNeighbors functions were used to create UMAP and nearest neighbor graphs, with the "reduction" parameter set to "harmony", and Findclusters function was used for Louvain clustering, with the resolution parameter set to 1.2. Finally, the clustering results were projected onto UMAP for visualization[53]. We used the FindAllMarkers function of Seurat (Wilcoxon rank-sum test and Bonferroni correction for multiple testing; adjusted $p < 0.05$) to identify marker genes for each cluster, with a minimum percentage of detected genes in at least 25% of cells (min.pct = 0.25). Then, the top 20 marker genes with the highest differential fold change (avg_log_2FC) in each cluster were selected for cell type annotation

Cellular metabolic activity status identification and differential expression analysis

We calculated the fraction of labeled transcripts (labeled transcripts/total transcripts) per cell and mapped them onto the UMAP. Metabolic activity states can be inferred based on the distribution of the ratio of new RNA (labeled transcripts) cells, and subgroups with distinct metabolic activity states within the same cell type can be obtained. Then the FindMarkers function from Seurat package was used to perform differential gene analysis on the new RNA between different metabolic activity subgroups of PCT and PST cells in normal kidney tissue, including H-PCT, L-PCT, H-PST, and L-PST. Wilcoxon rank-sum test was used, and genes with a fold change (log_2FC) > 2 and an adjusted *P*-value < 0.05 (Bonferroni correction) between two subgroups were considered as differentially expressed genes (DEGs). Mitochondrial and ribosomal genes were excluded from the analysis. The DEGs that showed significant upregulation in the new RNA between cells with different metabolic activity states were visualized using the pheatmap R package. Then, these DEGs were subjected to GO enrichment analysis. The org.Mm.eg.db R package was used to convert mouse gene IDs, and the enrichGO function from the clusterProfiler package was used to perform Gene Ontology (GO) enrichment analysis (ont = 'BP') of differentially expressed genes. Finally, the ggplot2 package was used to visualize the pathways with adjusted *P*-values < 0.05 (Benjamini-Hochberg correction).

Analysis of single-cell regulon activity

SCENIC[41] was used to identify cellular states by recognizing co-expression modules based on TFs and target gene expression that contain TF-binding sites. First, the raw count matrices of both new and old RNA genes were filtered, retaining genes whose sum of expression levels exceeded 3% of the total number of cells and were expressed in more than 1% of cells. Then, GRNBoost (implemented in pySCENIC) was used to infer co-expression modules and calculate the weights between TFs and target genes. Target genes that did not show positive correlation (> 0.03) in each TF module were removed. Subsequently, RcisTarget (implemented in R SCENIC) was used to prune co-expression modules into biologically meaningful regulatory units (regulons). This step relied on gene-motif ranking by performing motif enrichment analysis on each co-expression module in the cisTarget database, retaining significantly enriched motifs, and scoring genes in the co-expression module based on the retained motifs (also based on the cisTarget database) to identify significantly high-scoring genes as regulons. Furthermore, AUCell (implemented in R SCENIC) was used to score the activity of each regulon in each cell based on the gene expression value. We conducted two-sided Wilcoxon rank-sum tests following Z-score standardization of gene regulatory network (GRN) activity across various cell types to assess the significance of transcription factor activity differences under distinct AKI conditions. TFs with fold change in average AUC value > 1.5 and adjusted P value < 0.05 were considered as having differential regulatory activity under different AKI conditions.

Single-cell RNA velocity analysis

To characterize the dynamics of H-PST cells in AKI based on standard RNA velocity (splicing-based), the bam files generated from the Drop-seq pipeline were loaded into dropEst pipeline which was applied for demultiplexing reads to separate spliced and unspliced reads. The parameter was set as "-m-V-b-f-LeiEIBA" and genome annotation (GRCm38) was used. Then RNA velocity analysis was performed using Dynamo[13] (https://github.com/aristoteleo/dynamo-release/). Two count matrices (based on spliced and unspliced RNA) were included as inputs, both of which contained 274 differentially expressed genes from H-PST cells of the high metabolism AKI tissue. The "auto" dynamic model was set for velocity calculation and the results were mapped to two-dimensional UMAP space. The streamline plot was visualized using default parameters. To describe the RNA velocity of PST cells during AKI based on the metabolic labeling method, counts matrix of new and old transcripts was used as input for dynamo to calculate time-resolved RNA velocity based on metabolic labeling. The dynamic model was set to "auto" and "NTR_vel" was set to "TRUE". To explore the metabolic dynamics of H-PST and L-PST cells of AKI, we obtained differential gene expression matrices for H-PST (274 genes) and L-PST cells (37 genes) using the Seurat package, based on time differences in AKI; these differential genes were identified from pairwise comparisons between different injury time treatments and the no-injury control.

Inferring cell-cell communication with CellChat

R package CellChat (v 1.6.1)[33] was applied to perform cell-cell communication analysis based on new RNA and old RNA, respectively. The analysis utilized the built-in mouse ligand-receptor database, employing a tri-mean thresholding method to select significant interactions. Ligand–receptor interaction databases, including 'Secreted Signaling', 'ECM-Receptor', 'Cell–Cell Contact', were further applied for downstream analyses. The computation of communication probability was executed using the 'computeCommunProb' function. To identify global communication patterns, the 'selectK' function was used, and nPatterns = 4 was applied to determine the number of patterns for both incoming and outgoing communication. Additionally, the 'netAnalysis_signalingRole_network' function was utilized to visualize the corresponding signaling pathway role heatmap results.

Statistics & reproducibility

No statistical method was used to predetermine sample size. No data were excluded from the analyses. For the metabolically labeled kidney samples, there are two replicates for normal kidneys and kidneys with injury at 30 min, 3.8 h, and 5.3 h. However, for the non-metabolically labeled normal kidney samples and kidneys with injury at 50 min, there is only one replicate due to scale and cost constraints. To estimate the fraction of new transcripts, we randomly selected 100,000 consensus sequences at each time point. These sequences were used to compute the parameters p and q in the binomial mixture model. Investigators were blinded to allocation during experiments and outcome assessment.

Reporting summary

Further information on research design is available in the Nature Portfolio Reporting Summary linked to this article.

Data availability

The sequencing data generated in this study have been deposited in the Expression Omnibus (GEO) database under accession code GSE253836. Source data are provided with this paper.

Code availability

The source code for the analysis of Dyna-vivo-seq data is available on GitHub (https://github.com/guoye-ye/Dyna-vivo-seq/).

References

1. Bendall, S. C. et al. Single-cell trajectory detection uncovers progression and regulatory coordination in human B cell development. *Cell* **157**, 714–725 (2014).
2. Ding, J., Sharon, N. & Bar-Joseph, Z. Temporal modelling using single-cell transcriptomics. *Nat. Rev. Genet.* **23**, 355–368 (2022).
3. Macosko, E. Z. et al. Highly parallel genome-wide expression profiling of individual cells using nanoliter droplets. *Cell* **161**, 1202–1214 (2015).
4. Picelli, S. et al. Smart-seq2 for sensitive full-length transcriptome profiling in single cells. *Nat. Methods* **10**, 1096–1098 (2013).
5. Tang, F. et al. mRNA-Seq whole-transcriptome analysis of a single cell. *Nat. Methods* **6**, 377–382 (2009).
6. Chen, W. et al. Live-seq enables temporal transcriptomic recording of single cells. *Nature* **608**, 733–740 (2022).
7. Cao, J. et al. The single-cell transcriptional landscape of mammalian organogenesis. *Nature* **566**, 496–502 (2019).
8. Setty, M. et al. Wishbone identifies bifurcating developmental trajectories from single-cell data. *Nat. Biotechnol.* **34**, 637–645 (2016).
9. Moris, N., Pina, C. & Arias, A. M. Transition states and cell fate decisions in epigenetic landscapes. *Nat. Rev. Genet.* **17**, 693–703 (2016).
10. La Manno, G. et al. RNA velocity of single cells. *Nature* **560**, 494–498 (2018).
11. Bergen, V., Lange, M., Peidli, S., Wolf, F. A. & Theis, F. J. Generalizing RNA velocity to transient cell states through dynamical modeling. *Nat. Biotechnol.* **38**, 1408–1414 (2020).
12. Bergen, V., Soldatov, R. A., Kharchenko, P. V. & Theis, F. J. RNA velocity—current challenges and future perspectives. *Mol. Syst. Biol.* **17**, e10282 (2021).
13. Qiu, X. et al. Mapping transcriptomic vector fields of single cells. *Cell* **185**, 690–711.e645 (2022).
14. Battich, N. et al. Sequencing metabolically labeled transcripts in single cells reveals mRNA turnover strategies. *Science* **367**, 1151–1156 (2020).

15. Rabani, M. et al. Metabolic labeling of RNA uncovers principles of RNA production and degradation dynamics in mammalian cells. *Nat. Biotechnol.* **29**, 436–442 (2011).
16. Sun, M. et al. Comparative dynamic transcriptome analysis (cDTA) reveals mutual feedback between mRNA synthesis and degradation. *Genome Res* **22**, 1350–1359 (2012).
17. Herzog, V. A. et al. Thiol-linked alkylation of RNA to assess expression dynamics. *Nat. Methods* **14**, 1198–1204 (2017).
18. Su, L. et al. A bifunctional chemical signature enabling RNA 4-thiouridine enrichment sequencing with single-base resolution. *Chem. Commun.* **58**, 1322–1325 (2022).
19. Su, L. et al. Addition–Elimination Mechanism-Activated Nucleotide Transition Sequencing for RNA Dynamics Profiling. *Anal. Chem.* **93**, 13974–13980 (2021).
20. Qiu, Q. et al. Massively parallel and time-resolved RNA sequencing in single cells with scNT-seq. *Nat. Methods* **17**, 991–1001 (2020).
21. Erhard, F. et al. scSLAM-seq reveals core features of transcription dynamics in single cells. *Nature* **571**, 419–423 (2019).
22. Hendriks, G.-J. et al. NASC-seq monitors RNA synthesis in single cells. *Nat. Commun.* **10**, 3138 (2019).
23. Cao, J., Zhou, W., Steemers, F., Trapnell, C. & Shendure, J. Sci-fate characterizes the dynamics of gene expression in single cells. *Nat. Biotechnol.* **38**, 980–988 (2020).
24. Lake, B. B. et al. An atlas of healthy and injured cell states and niches in the human kidney. *Nature* **619**, 585–594 (2023).
25. Mehta, R. L. et al. International Society of Nephrology's 0by25 initiative for acute kidney injury (zero preventable deaths by 2025): a human rights case for nephrology. *Lancet* **385**, 2616–2643 (2015).
26. Xiao, Z. et al. Emerging early diagnostic methods for acute kidney injury. *Theranostics* **12**, 2963 (2022).
27. Kellum, J. A. et al. Acute kidney injury. *Nat. Rev. Dis. Prim.* **7**, 52 (2021).
28. Cippà, P. E. et al. Transcriptional trajectories of human kidney injury progression. *JCI insight* **3**, e123151 (2018).
29. Yin, K. et al. Well-Paired-Seq2: High-Throughput and High-Sensitivity Strategy for Characterizing Low RNA-Content Cell/Nucleus Transcriptomes. *Anal. Chem.* **96**, 6301–6310 (2024).
30. Lin, S. et al. Well-TEMP-seq as a microwell-based strategy for massively parallel profiling of single-cell temporal RNA dynamics. *Nat. Commun.* **14**, 1272 (2023).
31. Moqtaderi, Z., Geisberg, J. V. & Struhl, K. A compensatory link between cleavage/polyadenylation and mRNA turnover regulates steady-state mRNA levels in yeast. *Proc. Natl Acad. Sci.* **119**, e2121488119 (2022).
32. Buccitelli, C. & Selbach, M. mRNAs, proteins and the emerging principles of gene expression control. *Nat. Rev. Genet.* **21**, 630–644 (2020).
33. Jin, S. et al. Inference and analysis of cell-cell communication using CellChat. *Nat. Commun.* **12**, 1088 (2021).
34. Sato, Y., Takahashi, M. & Yanagita, M. in Seminars in Nephrology, Vol. 40 206–215 (Elsevier, 2020).
35. Shiva, N., Sharma, N., Kulkarni, Y. A., Mulay, S. R. & Gaikwad, A. B. Renal ischemia/reperfusion injury: An insight on in vitro and in vivo models. *Life Sci.* **256**, 117860 (2020).
36. Li, H., Dixon, E. E., Wu, H. & Humphreys, B. D. Comprehensive single-cell transcriptional profiling defines shared and unique epithelial injury responses during kidney fibrosis. *Cell Metab.* **34**, 1977–1998.e1979 (2022).
37. Zhang, Y. et al. Single-cell analyses of renal cell cancers reveal insights into tumor microenvironment, cell of origin, and therapy response. *Proc. Natl Acad. Sci.* **118**, e2103240118 (2021).
38. Yao, W. et al. Single cell RNA sequencing identifies a unique inflammatory macrophage subset as a druggable target for alleviating acute kidney injury. *Adv. Sci.* **9**, 2103675 (2022).
39. Gerhardt, L. M., Liu, J., Koppitch, K., Cippà, P. E. & McMahon, A. P. Single-nuclear transcriptomics reveals diversity of proximal tubule cell states in a dynamic response to acute kidney injury. *Proc. Natl Acad. Sci.* **118**, e2026684118 (2021).
40. Kirita, Y., Wu, H., Uchimura, K., Wilson, P. C. & Humphreys, B. D. Cell profiling of mouse acute kidney injury reveals conserved cellular responses to injury. *Proc. Natl Acad. Sci.* **117**, 15874–15883 (2020).
41. Aibar, S. et al. SCENIC: single-cell regulatory network inference and clustering. *Nat. Methods* **14**, 1083–1086 (2017).
42. Gobe, G. C. & Johnson, D. W. Distal tubular epithelial cells of the kidney: Potential support for proximal tubular cell survival after renal injury. *Int. J. Biochem. cell Biol.* **39**, 1551–1561 (2007).
43. Kang, H. M. et al. Defective fatty acid oxidation in renal tubular epithelial cells has a key role in kidney fibrosis development. *Nat. Med.* **21**, 37–46 (2015).
44. Bildirici, I. et al. PLIN2 is essential for trophoblastic lipid droplet accumulation and cell survival during hypoxia. *Endocrinology* **159**, 3937–3949 (2018).
45. Piret, S. E. & Mallipattu, S. K. Proximal tubular transcription factors in acute kidney injury: Recent advances. *Nephron* **144**, 613–615 (2020).
46. Yamaguchi, J., Tanaka, T., Eto, N. & Nangaku, M. Inflammation and hypoxia linked to renal injury by CCAAT/enhancer-binding protein δ. *Kidney Int.* **88**, 262–275 (2015).
47. Sun, J. et al. USF2 knockdown downregulates THBS1 to inhibit the TGF-β signaling pathway and reduce pyroptosis in sepsis-induced acute kidney injury. *Pharmacol. Res.* **176**, 105962 (2022).
48. Dobin, A. et al. STAR: ultrafast universal RNA-seq aligner. *Bioinformatics* **29**, 15–21 (2013).
49. Young, M. D. & Behjati, S. SoupX removes ambient RNA contamination from droplet-based single-cell RNA sequencing data. *Gigascience* **9**, giaa151 (2020).
50. McGinnis, C. S., Murrow, L. M. & Gartner, Z. J. DoubletFinder: doublet detection in single-cell RNA sequencing data using artificial nearest neighbors. *Cell Syst.* **8**, 329–337. e324 (2019).
51. Butler, A., Hoffman, P., Smibert, P., Papalexi, E. & Satija, R. Integrating single-cell transcriptomic data across different conditions, technologies, and species. *Nat. Biotechnol.* **36**, 411–420 (2018).
52. Korsunsky, I. et al. Fast, sensitive and accurate integration of single-cell data with Harmony. *Nat. Methods* **16**, 1289–1296 (2019).
53. Wu, T. et al. clusterProfiler 4.0: A universal enrichment tool for interpreting omics data. *The Innovation* **2**, 100141 (2021).

Acknowledgements

This work was supported by the National Natural Science Foundation of China (22293031), the Scientific Research Foundation of Xiang An Biomedicine Laboratory (2023XAKJ0100080), and the innovative research team of high-level local universities in Shanghai(SSMU-ZLCX20180701) to C.Y., the National Natural Science Foundation of China (22404106) and Postdoctoral Fellowship Program of CPSF (GZC20241035) to K.Y., the National Natural Science Foundation of China (22104080) and National Key R&D Program of China (2022YFA1104200) to J.S.

Author contributions

K.Y. and C.Y. designed this study. K.Y., Y.X., Z.Z., and M.Z. performed and analyzed experiments and drafted the manuscript. Y.G. and X.L. contributed to the data analysis. H.D., and D.L. contributed to the experiment analysis. C.Y., J.S., S.L., and J.Z. supervised the research and revised the manuscript. Z.Z. revised the manuscript. All authors discussed and commented on the results.

Competing interests

The authors declare no competing interests.

Additional information

Supplementary information The online version contains supplementary material available at https://doi.org/10.1038/s41467-024-54202-4.

Correspondence and requests for materials should be addressed to Junhua Zheng, Shichao Lin, Jia Song or Chaoyong Yang.

Peer review information *Nature Communications* thanks the anonymous reviewers for their contribution to the peer review of this work. A peer review file is available.